Journal of Petroleum Science and Engineering 208 (2022) 109603

Contents lists available at ScienceDirect

Journal of Petroleum Science and Engineering

journal homepage: www.elsevier.com/locate/petrol

Influence of water on elastic deformation of coal and its control on permeability in coalbed methane production

Junqiang Kang [a,b], Derek Elsworth [b], Xuehai Fu [a,*], Shun Liang [c], Hao Chen [d]

[a] Key Laboratory of Coalbed Methane Resources and Reservoir Formation Process, Ministry of Education, China University of Mining and Technology, Xuzhou, Jiangsu 221008, China
[b] Energy and Mineral Engineering, G3 Center and EMS Energy Institute, Pennsylvania State University, University Park, PA, USA
[c] School of Mines, Key Laboratory of Deep Coal Resource Mining, Ministry of Education of China, China University of Mining and Technology, Xuzhou, China
[d] PetroChina Research Institute of Petroleum Exploration and Development, Beijing 100083, China

ARTICLE INFO

Keywords:
Coalbed methane
Elastic deformation
Water saturation
Permeability

ABSTRACT

The permeability of the coal reservoir is affected by the stress caused by water production and matrix shrinkage caused by methane desorption, and its change rate is mainly affected by the elastic parameters of coal, namely Young's modulus (E) and Poisson's ratio (ν). E and ν will change with the change of coal water saturation, which will affect the reservoir permeability, but there is little research on it. Therefore, in this study, triaxial compression experiments were carried out on high volatility bituminous coal samples with different water saturation to obtain the variation law of E and ν with water saturation. Combined with gas permeability experiments of coal samples with different water saturation and finite element method, the influence of E and ν on permeability change were analyzed based on the P&M permeability evolution model. The results showed that E decreases linearly with the increase of water saturation, while ν increases linearly, and the change rate was affected by the fracture of coal and stress. The existence of fractures makes the mechanical properties of coal show great heterogeneity, resulting in the reduction of water action, and the stress will close the fractures to be as a whole, more prone to elastic deformation and greater deformation. The change of E and ν will lead to a decrease of permeability faster or slower, which depends on the initial E and ν and their change rate. Because the effects of E and ν on permeability are different and nonlinear, the control effects of E and ν on permeability are also different, depending on the E and ν value. The quantitative numerical analysis showed that the variation of E can increase permeability change range by at least 32%. When the E is less than 3000 MPa and greater than 4000 MPa, the influence degree is greater, more than 60%, which means that the change of E has a significant control effect on permeability change. The change of ν has little effect on the permeability change range with the maximum permeability change range is only 31%. The permeability of coal reservoir generally exceeds 3000 MPa, which means that more attention should be paid to the influence of E and ν change with water production on permeability, especially the change of E.

1. Introduction

Coalbed methane is an important unconventional energy source. Many countries with rich coalbed methane (CBM) resources around the world have carried out a lot of research on CBM development, including China (Qin et al., 2018), India (Chatterjee and Pal, 2010; Chatterjee and Paul, 2013; Ali et al., 2017), Canada (Gunter et al., 1997; Beaton et al., 2006), the United States (Green et al., 2008), Australia (Li et al., 2008) and Poland (Kędzior, 2009). Due to the differences of reservoirs in different regions, predecessors have conducted a lot of fine research on the production process of CBM is conductive to the effective development (Kędzior, 2009; Qin et al., 2018; Sinha and Gupta, 2021). CBM production involves methane desorption and migration driven by depressurization, in which dewatering plays a key role (Sun et al., 2017; Qin et al., 2018; Karthikeyan et al., 2020; Banerjee and Chatterjee, 2021). Water production not only affects the depressurization efficiency (Hamawand et al., 2013), but also causes a change in the elastic parameters of the coal, and change permeaiblity (Perera et al., 2011;

* Corresponding author. Room 345 of Key Laboratory of Coalbed Methane Resources and Reservoir Formation Process, China university of mining and technology, Jinshan East road, Xuzhou, Jiangsu province 221000, China.
E-mail address: fuxuehai@cumt.edu.cn (X. Fu).

https://doi.org/10.1016/j.petrol.2021.109603
Received 6 April 2021; Received in revised form 19 August 2021; Accepted 1 October 2021
Available online 6 October 2021

Vishal et al., 2015; Yao et al., 2015, 2016). Any resulting change of permeability greatly affects the efficiency of CBM production. In most current evolution models of permeability, E and ν are necessary parameters (Gray, 1987; Palmer and Mansoori, 1996; Shi and Durucan, 2004, 2005; Connell et al., 2010; Chatterjee et al., 2019). The permeability change in CBM production is mainly caused by the elastic deformation of the coal caused by stress and methane desorption (Sun et al., 2017). E and ν significantly affect the amplitude of deformation. Therefore, knowledge of the dynamic evolution of these parameters is necessary to accurately determine the dynamic change in permeability and in turn to define CBM production.

The influence of water on the mechanical parameters of various rocks (Yu et al., 1993; Vasarhelyi and Van, 2006; Lai et al., 2016; Roy et al., 2017) and of coal (Perera et al., 2011; Vishal et al., 2015; Yao et al., 2015, 2016; Chen et al., 2017, 2019; Sampath et al., 2018; Gu et al., 2019) has been a topic of some interest. An increase in water saturation can reduce the compressive strength and Young's modulus (E) of Australian coals (Perera et al., 2011) on the order of 10–20%. The uniaxial compressive strengths of Indian coking coal (Vishal et al., 2015) reduce by 7–25% and E by 32–38% as the sample is wetted to a 100% water saturation. The degree of fracture development is the main reason for the impact of water saturation. Uniaxial compressive strength (Yao et al., 2015, 2016) of Chinese long flame coal and fat coal show that an amplified plastic deformation appeared in the stress-strain curve with increasing water saturation. Compressive strength is linearly inversely-proportional to water saturation and E is exponentially inversely-proportional to water saturation. Compared to 0% saturation, compressive strength at 100% water saturation decreased by ~60%, and E decreases by ~50%. Saltwater decreases compressive strength by ~40% (Sampath et al., 2018). Tri-axial strength of anthracite under different confining pressures shows a reduction of ~40% with water saturation (Wang et al., 2018) at all confining pressures. Previous studies have shown that the water in coal significantly affects the mechanical properties, like reducing the fracture strength and Young's modulus and increase Poisson's ratio; in general, water will reduce the coal strength and make the coal more prone to deformation and fracture because water can dissolve some organic matter and clay minerals in the coal, resulting in the softening of coal bonding structure (Yu et al., 1993; Vasarhelyi and Van, 2006). For example, after the material in coal dissolve in water, corrosion cavities will be formed, resulting in easier compression of coal under stress to reduce the strength of coal. Moreover, water will adsorb the surface of the coal matrix, resulting in the reduction of the surface energy of the coal matrix. The reduction of the surface energy will reduce the stress required for the fracture of the coal reservoir, resulting in the reduction of the connection strength of matrix (Griffith, 1921).

The main research point of predecessors are the change in mechanical parameters between the extreme of 0–100% saturation (Perera et al., 2011; Vishal et al., 2015; Wang et al., 2018) relevant to coal mining (Yao et al., 2015; Wang et al., 2018) and gas storage in reservoirs (Perera et al., 2011; Vishal et al., 2015) but ignored intermediate saturations. However, water saturations decrease continuously in CBM production (Sun et al., 2017; Kang et al., 2018) requiring knowledge of behavior at intermediate saturations - that may endure for long periods. Thus, it is important to characterize the evolution of elastic parameters under different water saturation. However, there are relatively few studies (Perera et al., 2011; Yao et al., 2015, 2016) at intermediate saturations, especially for the Poisson's ratio (ν). Compared with other rocks, coal reservoirs develop natural fractures with specific form and shape (Laubach et al., 1998; Dawson and Esterle, 2010) and that exert a important influence on the mechanical properties of coal (Jaeger et al., 2009), requiring that their impact on mechanical response is accommodated.

We examined the response of two high volatility bituminous coals with different fracture development. The samples are from Xinjiang, China's largest deposits of low-strength and low-rank coals (Qin et al., 2018), which are also a focus for CBM development (Kang et al., 2018; Fu et al., 2016). The E and ν of six groups (36 samples) were determined by triaxial compression experiments at different confining pressures and supplemented by four groups (16 samples) of gas permeability experiments, all at different water saturation. Relationships between water saturation, E and ν were established, and the influence of water saturation on permeability was analyzed qualitatively and quantitatively according to the P&M permeability evolution model (Palmer and Mansoori, 1996).

2. Samples and experiments

High volatility bituminous coals from two mining areas were used for triaxial compression and gas permeability experiments at different water saturation to explore the influence of water saturations on E and ν and to link this change in mechanical characteristics on permeability evolution.

2.1. Samples preparation

The coal samples of the research from Fukang mine (FK) and Tongtai mine (TT) in China Xinjiang were used in this study (Cheng et al., 2020). All samples were collected from a fresh coal face. 50 × 100 mm cores were drilled along the bedding direction for the triaxial compression experiments (Ulusay, 2014) and 25 × 50 mm cylinders were used for the permeability measurements. Separate samples are recovered for the triaxial compression experiments from a single 300 mm × 300 mm × 200 mm block sample - avoiding large variation in properties.

Analyses of samples were based on ISO-17-246-2005 for maximum vitrinite reflectance and ISO-7404-5-2009 for macerals. Both coals are high volatility bituminous coals with TT comprising principally inertinite and FK principally vitrinite (Table 1). Compared with the two samples, the TT contains more fractures than FK samples (Fig. 1a and b), which can be used to study the mechanical characteristics of coal samples with different fracture development degrees.

2.2. Water saturation treatment and experiment

1) Sample water saturation treatment

The initial moisture of the samples were removed by drying at 60 °C for 24 h and then weighed (Liu et al., 2020). After weighing, the samples were saturated with 48 h of 10 MPa in distilled water then reweighed. The purpose of this is to obtain the sample mass after water saturation and to control water saturation. The weight of the target water saturation is defined as:

$$m_g = (m_s - m_0) \times S_w + m_0 \quad (1)$$

where m_g is the sample mass in the target water saturation, g; m_s is the sample mass in 100% water saturation (sample saturated for 48 h), g; m_0 is the dry sample mass, g; S_w is the target water saturation. According to the weight desired for the target water saturation, the samples were naturally dried at room temperature (approximately 25 °C) and the weight monitored in real-time to define water saturation. The natural drying time of each sample is less than 24 h, so the influence of the drying process on the sample can be ignored.

Table 1
Analysis of macerals and $R_{o,max}$ of samples FK and TT.

No.	Proximate analysis			Maceral			$R_{o,max}$%
	*M*ad/ %	*A*d/ %	*V*daf/ %	Vitrinite %	Inertinite %	Liptinite %	
TT	3.12	4.95	31.42	18.58	79.78	1.64	0.34
FK	1.56	4.55	23.84	79.80	18.70	0.60	0.64

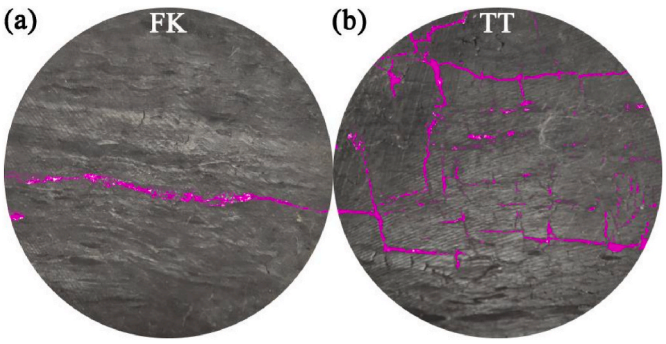

Fig. 1. Cross-sectional view of fractures in the undeveloped and fracture-developed samples. (a): Sample FK with a continuous smooth section. (b): Sample TT with clear fractures. Fractures include natural fractures and water-loss-generated shrinkage fractures.

2) Triaxial compression experiments

Triaxial compression tests were carried out immediately after water treatment on an MTS-815 high-pressure tri-axial test rig (Fig. 2). The sample was wrapped with rubber tape then sealed with thermoplastic tape against the confining fluid (oil). A 1 KN seating force was applied to the seat of the sample, then attached a radial strain gauge. After preparation, the confining vessel is applied and the confining pressure slowly increased to the target pressure. Then axial stress is applied to a constant axial displacement rate of 0.1 mm/min until the sample ruptures. A total of 36 samples of 6 groups were tested (Table 2). Using the stress-strain curve, E and ν of each sample can be calculated (Liu et al., 2020).

3) Gas permeability experiments

Four samples (FK-1, FK-2, TT-1, TT-2) were selected for permeability experiments. Each sample was elevated to four different water saturations for a total of 16 gas permeability tests (Table 3). The permeability is significantly reduced by the water so these are limited to a maximum saturation of <70%. Because the initial permeability of each sample is different, the permeability of some samples is very low in high water saturation, so it is hard to accurately measure the permeability. Therefore, the water saturation set by each sample was different to ensure the accurate measurement of permeability. Permeability was measured in a PDP-200 pulse unsteady state permeability apparatus from Core Labs Inc (Kang et al., 2018). The unsteady-state method effectively prevents changes in water saturation during permeability measurements (Zhang et al., 2019).

The permeability test experimental conditions are that the pore nitrogen pressure is 2 MPa with less than 0.1 MPa error. The confining pressure is 4–12 MPa with less than 0.1 MPa error (5 pressure points, each pressure interval is 2 MPa) (Table 3). After putting the sample into the core holder, input the confining pressure and pore nitrogen pressure set in Table 3 into the computer. A 20psi (0.14 MPa) gas pulse will be applied to one end of the core holder when the air pressure is stable. Under the action of pulse, the calculated permeability value will continue to drop to a stable value, which is the permeability at this pressure point (Jones, 1972; Freeman and Bush, 1983). The criterion of stable permeability value is the ratio of the difference between real-time

Table 2
Tri-axial compression experiment parameters for coal samples at different water saturations.

No.	Water saturation/%	Confining pressure/MPa	Fractures
FK	0, 20, 40, 60, 80, 100	10	Undeveloped fracture
		15	
		20	
TT		10	Developed fracture
		15	
		20	

Table 3
Permeability test parameters for coal samples.

No.	Water saturation/%	Effective pressure/MPa
FK-1	0, 35, 41, 66	2, 4, 6, 8, 10
FK-2	0, 21, 35, 45	
TT-1	0, 32, 53, 68	
TT-2	0, 22, 48, 59	

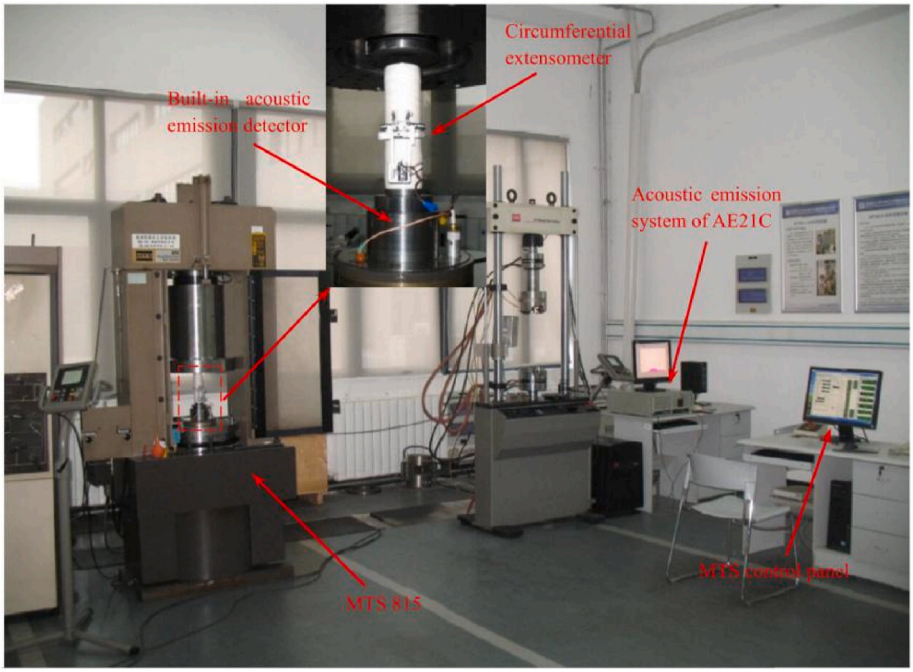

Fig. 2. Tri-axial mechanical experimental system (Wu et al., 2018).

permeability and average permeability within 1 min. If the average permeability is less than 1%, the permeability is considered to be stable. When the first pressure point is tested, the confining pressure will increase automatically according to the setting of the next pressure point.

3. Results and discusses

In the following, the elastic deformation of the coals at different water saturations were characterized by triaxial compression and gas permeability experiments. The triaxial compression experiments directly measure the change in E and ν with water saturation, while the gas permeability experiment indirectly reflects elastic deformation through the observed changes in permeability with water saturation. Based on the results, the influence of dynamic changes in E and ν on permeability were analyzed qualitatively and quantitatively based on the P&M permeability model and finite element method.

3.1. The E and ν changes with water saturation

The E and ν reflect the elastic deformational properties of the coal (Jaeger et al., 2009), which are also involved in CBM production. From the experimental results, E decreased linearly with increase of water saturation, while the ν was the opposite (Figs. 3 and 4). Water in coal will dissolve organic matter and clay minerals, and reduce the surface chemistry potential energy of the coal, making the coal bond structure to soften (Yu et al., 1993; Vasarhelyi and Van, 2006), which leads to larger deformation under the given stress (Vutukuri et al., 1974). As a result, larger deformation occurs with increasing water saturation (Yao et al., 2015, 2016), representing a reduction in E (Fig. 3). The ν is a combined reflection of circumferential strain relative to axial strain. Because the strain of elastic deformation is far less than the sample size, the change amplitude of axial strain is lower than that of radial strain in little volume change (Vutukuri et al., 1974; Jaeger et al., 2009). Therefore, when the softening of water leads to the increase of axial strain, the increase of radial expansion is greater, so ν increases with the increasing water saturation.

The linear relationship of E and ν with water saturation were fitted (Figs. 3 and 4). The linear correlation coefficient (R^2) of TT samples with more fractures were slightly lower than that of the FK sample with fewer fractures (Figs. 3 and 4). Because of the fractures, E and ν of different samples are different under dry conditions, so E and ν of saturated water are difficult to match the results of other samples, so the R^2 was lower than that of samples with fewer fractures. There were few significantly abnormal data in FK and TT samples. This is because the influence of some fractures on E and ν is greater than that of water, which leads to significant anomalies in the data, and these abnormal data were not used for linear fitting.

The change rate of E and ν with water saturation can be obtained from the fitting equation (Fig. 5). The change rate is the ratio of the constant term to the coefficient of variation of the fitted linear equation, which represents the decrease of E or ν after 100% water saturation. The change rate of E ranged from 10% to 38%, with an average of 25.5%. The change rate of ν ranged from 50% to 113.3%, with an average of 72.6%. This indicates that E of dry samples will decrease by 25.5% and ν will increase by 72.6% after saturated by water. For CBM production, the changes in E and ν in the water production (water saturation continues to decline) will significantly affect the change of reservoir permeability, which will be discussed in the next section. There was no significant difference between the change rate of E of the FK samples and that of the TT samples, which is 22.1% and 30.0% respectively. However, the change rate of ν was significantly higher in FK samples than TT samples (Fig. 5). The average change rate of ν of FK sample is 92.2%, and that of TT sample is 52.9%. This is because the fractures are compressed during axial deformation, which makes the axial strain decrease (Jaeger et al., 2009). Comparing the change rates of E and ν under different confining pressures, it was found that the change rates of E and ν increase with the increase of confining pressure (Fig. 5). With the increase of confining pressure, coal will transform from brittle deformation to ductile deformation (Jaeger et al., 2009). The increase of confining pressure will increase the elastic strain process, and the softening of coal caused by moisture will get more extension, that is, greater deformation. This suggested that water has a greater influence on the elastic deformation of coal in high-stress areas.

3.2. Qualitative and quantitative analysis of the influence of E and ν on permeability during CBM production

3.2.1. Qualitative analysis of the influence of E and ν on permeability based on P&M permeability model

CBM production is a process of water production and pressure reduction (Zhou et al., 2020). The water production efficiency greatly affects the decline rate of reservoir pressure, and then affects the CBM production. However, water production will also lead to changes in reservoir mechanical properties, such as Young's modulus and Poisson's ratio (Figs. 3 and 4). The changes of Young's modulus and Poisson's ratio will significantly affect the deformation of coal, and then affect the permeability. Permeability is an important parameter for CBM production. Predecessors have also established a dozen numerical models (Pan and Connell, 2012). It is particularly important to select an appropriate model to qualitatively or quantitatively analyze the impact of aquatic products on permeability. In these permeability models, the P&M permeability model is one of the most widely used in field production and also in commercial oil and gas production software (Eclipse, 2018; CMG, 2019). Therefore, P&M model is used for the following qualitative

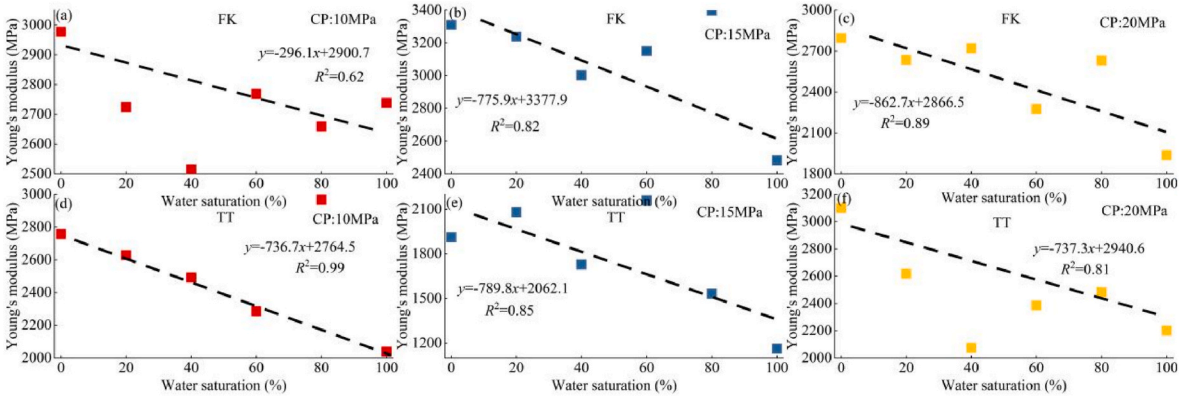

Fig. 3. Change of E for samples FK and TT with water saturation under different confining pressures. The fractures in sample FK were not well-developed while those in TT were more-developed.

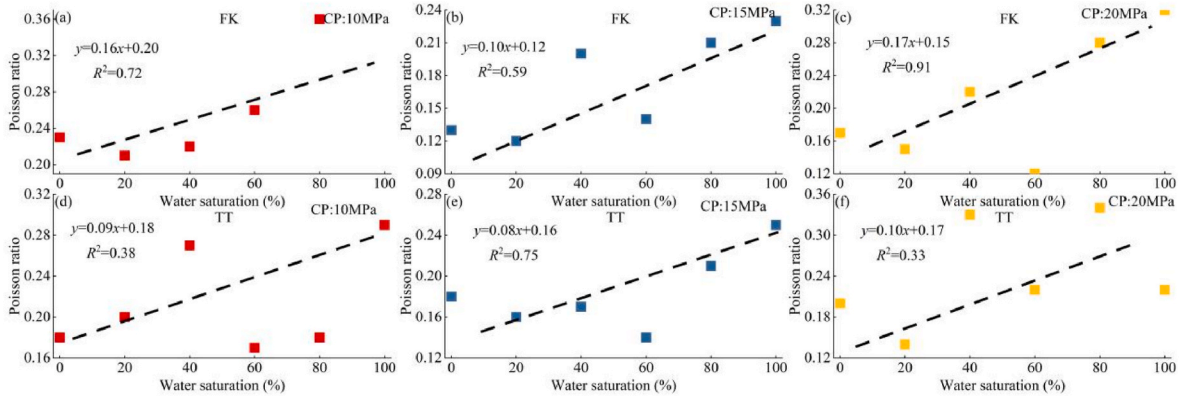

Fig. 4. Change in v for samples FK and TT with water saturation under different confining pressures. The fractures in sample FK were not well-developed while those in TT were more-developed.

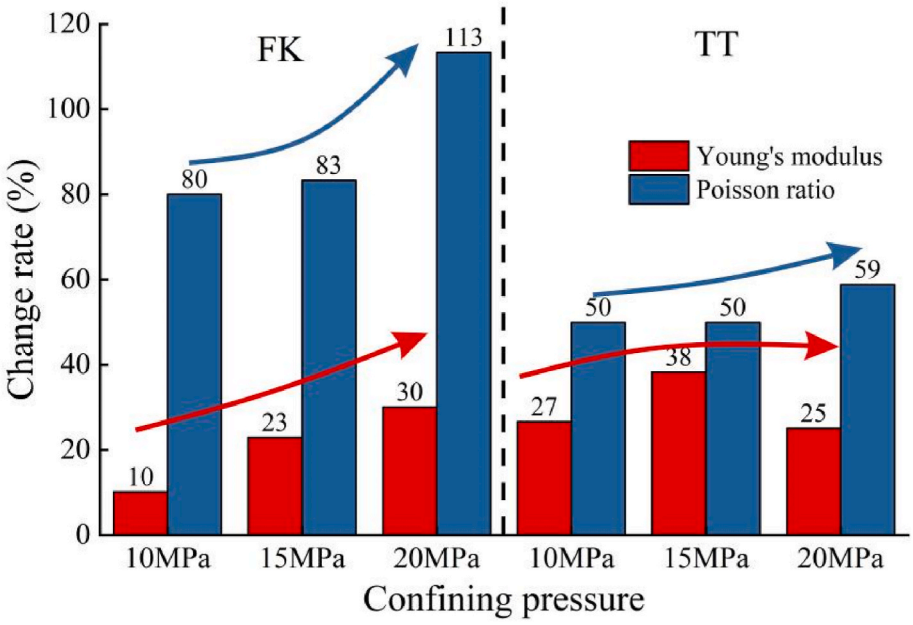

Fig. 5. The change rate of Young modulus and Poisson ratio. Note: CP-confine pressure in triaxial mechanical experiment

analysis, but this does not mean that the research results are only applicable to the P&M model. Permeability model comparison will be carried out in the next section to obtain more comprehensive results.

Based on the P&M permeability evolution model (Palmer and Mansoori, 1996):

$$K = K_0\left\{\overbrace{1}^{①} + \overbrace{\left[\frac{(1-2v)(1+v)}{E(1-v)\varphi_0}\right](p-p_0)}^{②} + \overbrace{\frac{1}{\varphi_0}\left[\frac{1}{3}\left(\frac{1+v}{1-v}\right)-1\right]\left(\frac{\varepsilon\beta p}{1+\beta p}-\frac{\varepsilon\beta p_0}{1+\beta p_0}\right)}^{③}\right\}^3 \tag{2}$$

where K is the permeability; K_0 is the initial permeability; p is the reservoir pressure; p_0 is the initial reservoir pressure; ε and β are the deformation parameters caused by methane desorption. The P&M equation is derived based on the uniaxial strain assumption (Palmer and Mansoori, 1996). Eq. (2) includes three items, in which ① represents the initial value, ② represents the decrease of permeability caused by the decrease of reservoir pressure, and ③ represents the increase of permeability caused by methane desorption. Because water production mainly occurs in the early stage of CBM production and methane production is very small (Kang et al., 2018, 2019; Zhou et al., 2020), then the permeability change caused by methane desorption strain may be ignored, that is ③ in Eq. (2) is ignored. Thus, Eq. (2) can be rewritten as:

$$k = k_0\left[1+\frac{(1-2v)(1+v)}{\varphi_0 E(1-v)}(p-p_0)\right]^3 \tag{3}$$

Eq. (3) only includes the decrease of permeability caused by the decrease of reservoir pressure. The experimental data above showed that E decreases linearly and that v increases linearly with increase of water

saturation, as:

$$\begin{aligned} v &= as_w + b(a > 0) \\ E &= cs_w + d(c < 0) \end{aligned} \tag{4}$$

Thus let $f(v,E)$ be:

$$f(v,E) = \frac{(1-2v)(1+v)}{E(1-v)} \tag{5}$$

So $f(s_w)$:

$$f(v,E) = \frac{(1-2(as_w+b))(1+as_w+b)}{(cs_w+d)(1-as_w-b)} \tag{6}$$

From Eq. (3), representing the early stages of CBM production, reservoir permeability gradually decreases with decreasing reservoir pressure, while $f(v,E)$ controls the decreased amplitude of permeability. According to Eq. (4) and (5), $1/E$ decreases monotonically with increasing water saturation, and $(1\text{-}2v)(1+v)/(1\text{-}v)$ increases monotonically in the range [0,0.5] of v, thus the changing trend of $f(v,E)$ cannot be seen with increasing water saturation decreases. The assumption of Eq. (3) is based on the initial stage of coalbed methane production, ignoring the permeability change caused by methane desorption. Although there is a large amount of water production at this stage, not all water is produced. From the on-site CBM production data, water production is approximately 60% of the total water production in the initial production stage (without a large amount of gas production) (Kang et al., 2018, 2019). Therefore, when the water saturation is greater than 40%, it is acceptable to ignore the change of permeability caused by methane desorption, and the minimum value of S_w in the below analysis is set to 40%. For on-site CBM production, the water production of different production areas at the initial stage is significantly different, so we only choose a general value here, not for a specific area. Because the purpose is to explore the general law of the influence of E and v on permeability caused by water change, and different water saturation range will not affect the permeability change trend, so we do not do in-depth consideration here.

The trend of $f(v,E)$ with water saturation was obtained by substituting Figs. 3 and 4 into Eq. (6) (Fig. 6). It can be seen that $f(v,E)$ differs between different samples (Fig. 6). It showed that with the decrease of water saturation, there are four figures showed that a decrease (Fig. 6b,d,e,f), one showed that an increase (Fig. 6a), and one showed that an increase first and then a decrease (Fig. 6c). If $f(v,E)$ increases with decreasing water saturation, the permeability will also decrease more slowly than that of permeability under E and v measured in dry condition ($f(0)$). Conversely, if $f(v,E)$ decreases with decreasing water saturation, the permeability decreases faster. The six distribution maps were projected into a three-dimensional distribution map of $f(v,E)$ (Fig. 7). This showed that v is small for the $f(v,E)$ decrease with decreasing water saturation (Fig. 7a). The lower v weakens the influence of v on the $f(v,E)$, while the change in E had a greater influence on $f(v,E)$. For $f(v,E)$ increase with decreasing water saturation (Fig. 7b), the v had a greater change with decreasing water saturation, and the change of E is smaller (Fig. 7b-af). This makes the change in v the dominant control. In Fig. 6c, the increase and then decrease of $f(v,E)$ is due to the change of the two parameters at their intersection, from v dominated to E dominated.

The above analysis can be further verified against gas permeability changes recorded under different water saturation. The data showed that permeability decreases gradually with increasing water saturation due to water hinders the flow of gases (Fig. 8). Effective stress and permeability are related as (Seidle et al., 1992):

$$k = k_0 e^{-3C_f(p-p_0)} \tag{7}$$

where k is gas permeability; k_0 is Klinkenberg permeability; C_f is fracture compression coefficient, p is confining pressure; p_0 is pore pressure. According to Eq. (2), the exponential relation between effective stress and permeability was used to fit the corresponding value of C_f. C_f is an index reflecting the relative change in permeability under a given stress change (Zhang et al., 2019). The fracture compression coefficient C_f is (Pan and Connell, 2012):

$$c_f = \frac{(1+v)(1-2v)}{(1-v)E\varphi} \tag{8}$$

Combining with Eq. (5):

$$f(v,E) = c_f \times \varphi_0 \times S_w \tag{9}$$

Based on the gas permeability data, the change in permeability as $f(v,E)$ for four samples under different water saturation can be obtained (Table 4, Fig. 9). It is clear that $f(v,E)$ increases with decreasing water saturation (Fig. 9), which is similar to Fig. 6a,c. Table 4 also showed that $f(v,E)$ decreased by more than 4% for every 10% change in water saturation. Comparing the relationship between the amplitude of change and the Klinkenberg permeability, it was found that the larger the permeability, the larger the change in permeability (Fig. 10). The four samples were from two mining areas, but each sample retained a significant difference in permeability due to the presence of fractures. Fractures reduce E, while the effect on v is small (Figs. 3 and 4). Therefore, for the samples containing fractures, that is, the samples with high permeability, the lower E makes $f(v,E)$ change significantly under the same change in water saturation (Zhang et al., 2019). Zhang's research also shows the same change trend (Zhang et al., 2019).

3.2.2. *Permeability change compared among different permeability change models*

Many permeability change evolution models have been established (Table 5; Gray, 1987; Sawyer et al., 1987; Harpalani and Chen, 1995;

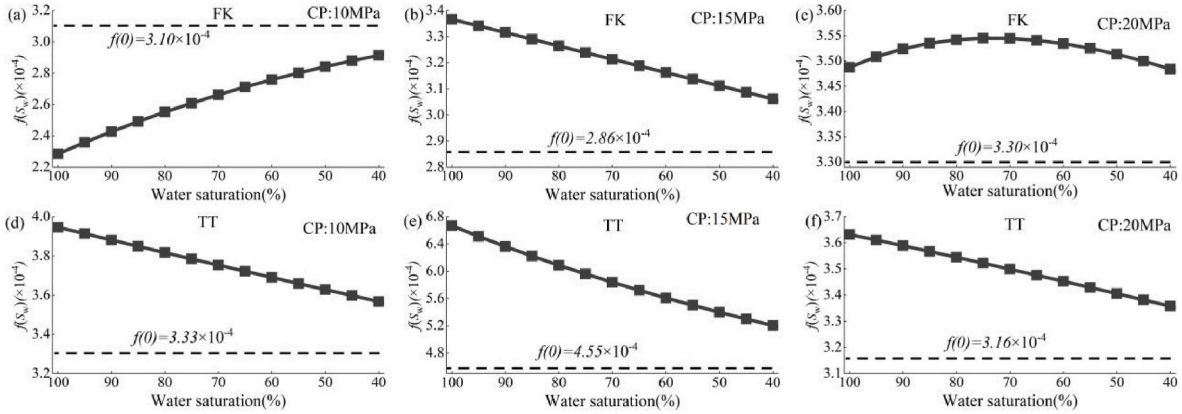

Fig. 6. Variation trend of $f(v,E)$ with water saturation $f(0)$ is the $f(S_w)$ value when the water saturation is 0, in order to better compare with the dry sample.

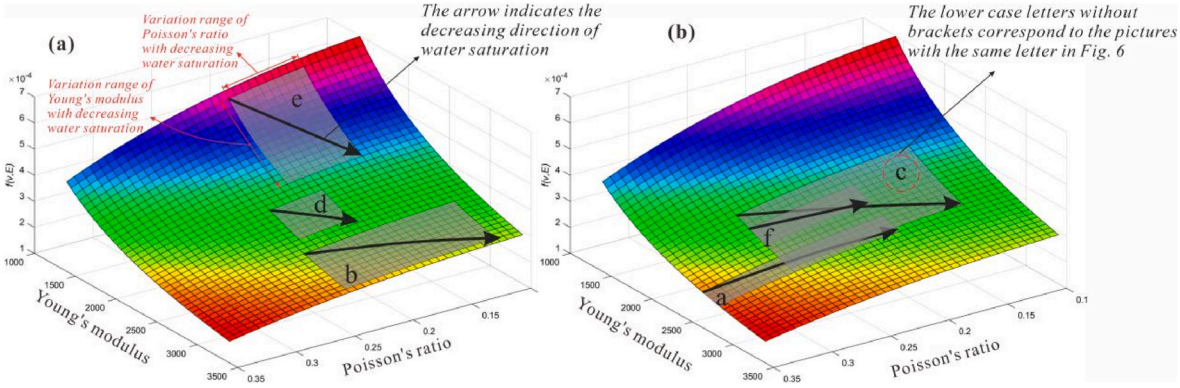

Fig. 7. Three spatial distributions of $f(v,E)$ with water saturation under different E and v. The secondary number in the figure corresponds to the number in Fig. 6.

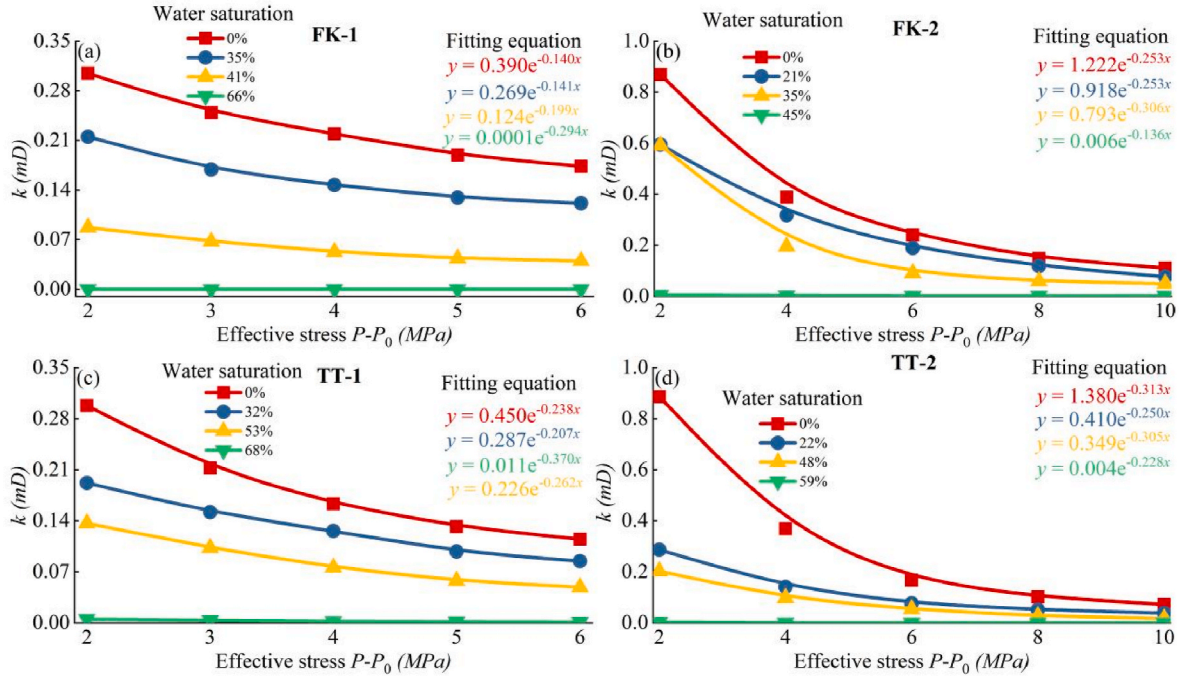

Fig. 8. Effective stress-permeability at different S_w.

Table 4
Change of $f(v,E)$ under different water saturation based on gas permeability calculation.

No.	S_w/ %	$f(v,E)$	$\Delta f(v,E)/\Delta 10\% S_w$	No.	S_w/ %	$f(v,E)$	$\Delta f(v,E)/\Delta 10\% S_w$
FK-1	0	0.0048	−4.38	TT-1	0	0.0065	−7.38
	35	0.0032			32	0.0038	
	41	0.0040			53	0.0034	
	66	0.0034			68	0.0032	
FK-2	0	0.0031	−15.62	TT-2	0	0.0082	−11.92
	21	0.0025			22	0.0051	
	35	0.0025			48	0.0041	
	45	0.0009			59	0.0025	

Levine, 1996; Palmer and Mansoori, 1996; Gilman and Beckie, 2000; Shi and Durucan, 2004, 2005; Cui and Bustin, 2005; Robertson and Christiansen, 2006; Liu and Rutqvist, 2010; Connell et al., 2010). The P&M model (Palmer and Mansoori, 1996) is one broadly used model. Summarizing the basic formula of the permeability models, permeability changes due to two competing features: (i) permeability decrease caused by the increase of effective stress due to water production and (ii)

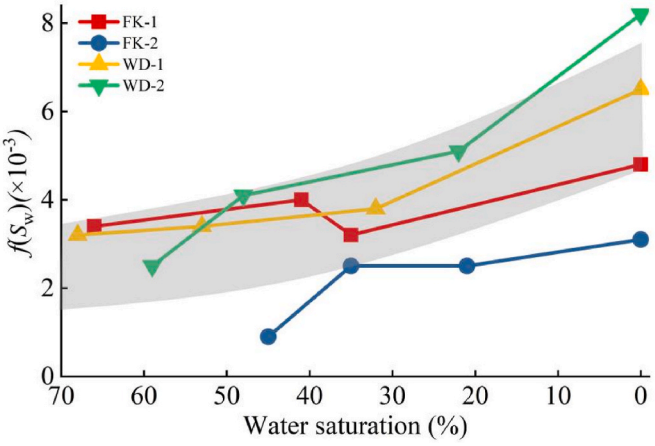

Fig. 9. Variation of $f(v,E)$ for different water saturation in four different permeability samples.

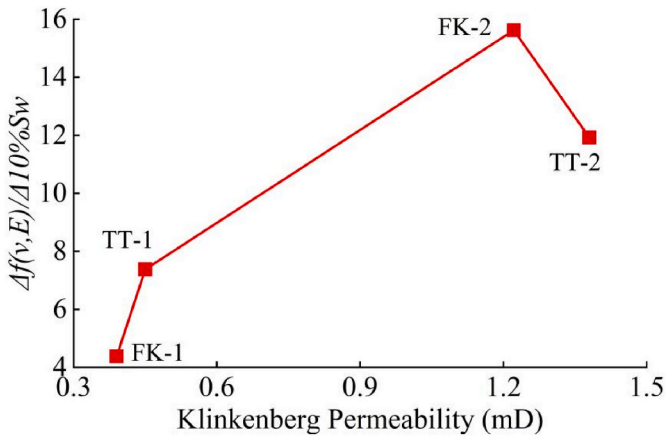

Fig. 10. Variation in the trend of $f(v,E)$ per 10% water saturation with Klinkenberg permeability.Note: CP-confine pressure in triaxial mechanical experiment

permeability increase caused by the methane desorption. The change in permeability with reservoir pressure can be summarized as:

$$K = K_0[-a(p-p_0)+\Delta\varepsilon_s+b]^3 \tag{10}$$

Where $\Delta\varepsilon_s$ is the desorption shrinkage due to methane desorption, b is the other parameters considered specifically, such as thermal effect, and a is the parameter related to coal mechanics. In the early stage of CBM production, methane desorption is relatively small, so only the decrease in permeability caused by water production is considered here. The expression representing effective stress effects has two forms (Table 5). The first form is (Sawyer et al., 1987; Palmer and Mansoori, 1996; Cui and Bustin, 2005; Connell et al., 2010):

$$a = f(v,E) = \frac{(1+v)(1-2v)}{E(1-v)} \tag{11}$$

and the second form is (Gray, 1987; Shi and Durucan, 2004, 2005; Gilman and Beckie, 2000; Liu and Rutqvist, 2010):

$$a = g(v,E) = \frac{v}{E(1-v)} \tag{12}$$

Eq. (11) and Eq. (12) are based on two different stress conditions under the uniaxial strain assumption, where Eq. (11) represents three-dimensional stress, while Eq. (12) only horizontal stress (Pan et al., 2010; Pan and Connell, 2012; Seidle, 2011). The most representative permeability models, based on Eq. (11) and Eq. (12) are a P&M model and an S&D model (Pan et al., 2010; Pan and Connell, 2012), respectively. When comparing permeability models, choosing more classical models is very helpful to obtain more reliable results. Eq. (11) and Eq. (11) reflect the basic framework under two stress assumptions, and most permeability models are established on this basis. Therefore, we compare the direct differences between the two formulas, and then we can include more core differences between many permeability models to obtain more reliable conclusions.

Using Eq. (12), the change of $g(v,E)$ with water saturation was obtained (Fig. 11). The $g(v,E)$ of the six groups samples gradually decreases as water saturation decreases, thus considering the changes in E and v, the permeability will drop faster than expected. This is not the same as the change of $f(v,E)$ with water saturation (Fig. 6). Plot $f(v,E)$ and $g(v,E)$ in the three-dimensional spatial distribution where E is [1000 6000] and v is [0.1 0.5]. The distribution trends of $f(v,E)$ and $g(v,E)$ are opposite (Fig. 12). The gas permeability result was consistent with the trend of $f(v,E)$ (Fig. 6), which showed that if considering the change of E and v with water saturation, the $f(v,E)$ model considering three-dimensional stress provides a better fit to observations. This is one of the reasons why the P&M model is widely embedded in commercial reservoir simulation software (Eclipse, 2018; CMG, 2019).

3.2.3. *Quantitative analysis of the influence of E and v on permeability*

Water saturation and permeability are linked in nonlinear two-way coupling feedback (Liu et al., 2011; Ma et al., 2017) requiring that numerical models were used to follow CBM production. We explored the impact of water production on reservoir permeability using finite element methods. Basic models of gas-water flow are available (Liu et al., 2011; Fan et al., 2019a, 2019b) that include three continuity flow equations, for methane flow in the matrix, methane flow in the fracture network, and water flow in the fracture network, together with the volume strain caused by the stress change. These relations are:

1) Methane flow in matrix

Methane in coal matrix includes free methane in matrix pores and

Table 5
Summary of permeability models during coalbed methane production.

Author(s)	Expressions	Stress environment
Gray (1987)	$\varepsilon_h^e-\varepsilon_{h0}^e=-\frac{v}{E(1-v)}(p-p_0)+\frac{1}{1-v}\frac{\Delta\varepsilon_s}{\Delta p_s}\Delta p_s$	Horizontal stress
Sawyer et al., 1987	$\varphi=\varphi_0\left[1+\frac{(1-2v)(1+v)}{E(1-v)\varphi_0}(p-p_0)\right]-c_m(1-\varphi_0)\frac{\Delta p_0}{\Delta C_0}[(C-C_0)+c_k(C_t-C)]$	Three-dimensional average stress
Harpalani and Chen, 1995	$\frac{k}{k_0}=\left(1+\frac{2l_m^*\Delta p}{\varphi_0}\right)^3/(1-l_m^*\Delta p), l_m^*\Delta p=-1+\sqrt{1+\varepsilon_1\left(\frac{Bp_0}{1+Bp_0}-\frac{Bp}{1+Bp}\right)}+\frac{1-v}{E}(p-p_0)$	Horizontal stress
Levine, 1996	$k=\frac{(1.013e10^9)b^3}{12a}, \frac{b}{a}=\frac{b_0}{a}+\frac{1-2v}{E}(p-p_0)+\frac{\varepsilon_l p_{50}}{(p_{50}+p)^2}(p-p_0)$	Horizontal stress
Palmer and Mansoori, 1996	$\varphi=\varphi_0\left\{\left[1+\frac{(1-2v)(1+v)}{E(1-v)\varphi_0}-\left(\frac{1}{3\varphi_0}\left(\frac{1+v}{1-v}\right)+f-1\right)\gamma\right](p-p_0)+\frac{1}{\varphi_0}\left[\frac{1}{3}\left(\frac{1+v}{1-v}\right)-1\right]\left(\frac{\varepsilon\beta p}{1+\beta p}-\frac{\varepsilon\beta p_0}{1+\beta p_0}\right)\right\}$	Three-dimensional average stress
Gilman and Beckie, 2000	$\frac{k}{k_0}=\exp\left(-\frac{3\Delta\sigma_x^e}{E_F}\right), \Delta\sigma_x^e=-\frac{v}{1-v}(p-p_0)+\frac{E}{1-v}\alpha_s\Delta S$	Horizontal stress
Shi and Durucan, 2004, 2005	$\sigma_h^e-\sigma_{h0}^e=-\frac{v}{1-v}(p-p_0)+\frac{E\varepsilon_s}{3(1-v)}$	Horizontal stress
Cui and Bustin, 2005	$\varphi=\varphi_0+\frac{(1-2v)(1+v)}{E(1-v)\varphi_0}(p-p_0)-\frac{2}{3}\left(\frac{1-2v}{1-v}\right)\Delta\varepsilon_s$	Three-dimensional average stress
Robertson and Christiansen, 2006	$\frac{k}{k_0}=\exp\left(3c_f\left(p-p_0\right)+\frac{9}{\varphi_0}\left[\frac{1-2v}{E}(p-p_0)-\frac{\varepsilon_{max}p_L}{p_L+p_0}\ln\left(\frac{p_L+p}{p_L+p_0}\right)\right]\right), c_f=\frac{c_0}{\alpha(\sigma-\sigma_0)}[1-e^{-\alpha(\sigma-\sigma_0)}]$	Three-dimensional average stress
Liu and Rutqvist, 2010	$\Delta\sigma=-\frac{v}{1-v}(p-p_0)+\frac{E}{1-v}(\Delta\varepsilon_s-\Delta\varepsilon_f), \Delta\varepsilon_f=\frac{1}{2}\varphi_0(1-e^{-c_f\Delta\sigma})$	Horizontal stress
Connell et al., 2010	$k=k_0\exp\left(-3\left[\frac{(1-2v)(1+v)}{E(1-v)}\left(\frac{1}{3}(2p_r+p_z)-p_p\right)-(1-\gamma)\varepsilon_s\right]\right)$	Three-dimensional average stress

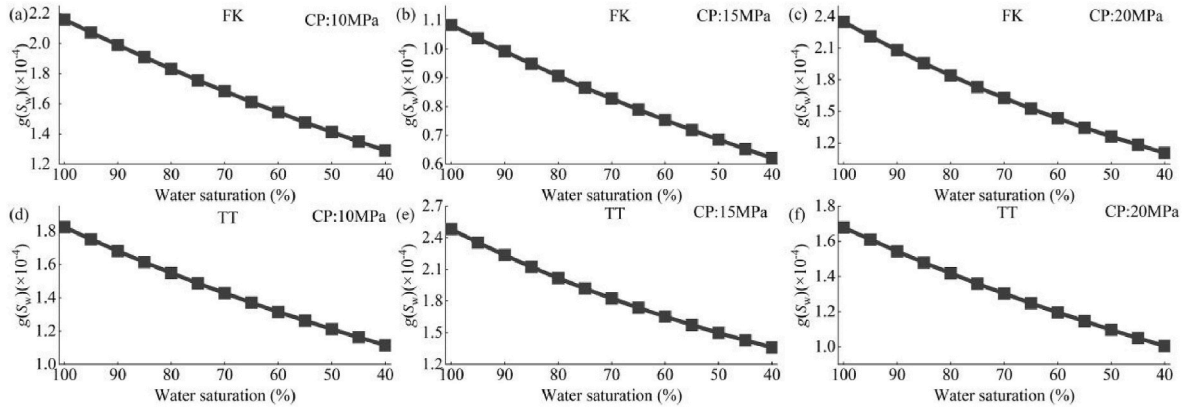

Fig. 11. The $g(v,E)$ change with decreasing water saturation.

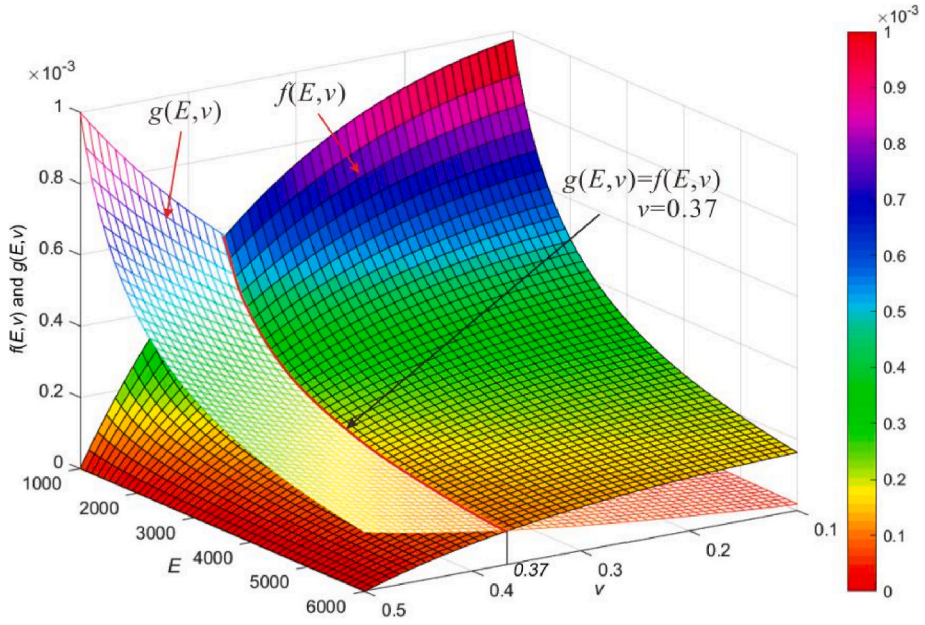

Fig. 12. The three-dimensional spatial distribution of $f(v,E)$ and $g(v,E)$. When $v = 0.37$, $f(v,E)$ and $g(v,E)$ are equal.

adsorbed methane on the matrix surface (Fan et al., 2019a, 2019b). According to the ideal gas equation and Langmuir adsorption theory, the methane density in the matrix is:

$$\overbrace{\rho_m}^{①} + \overbrace{\rho_{ad}}^{②} = \overbrace{\varphi_m \frac{M}{RT} p_{mg}}^{③} + \overbrace{\frac{V_L b_L p_{mg}}{1 + b_L p_{mg}} \rho_c \rho_{gs}}^{④} \tag{13}$$

Where ρ_m is free methane density in matrix, kg/m^3; ρ_{ad} is absorbed methane density in the matrix, kg/m^3; φ_m is matrix porosity; M is molar mass of methane, g/mol; R is the ideal gas constant, J/(mol·K), and; T is temperature, K. In Eq. (13), according to the law of mass conservation, methane in coal matrix can be divided into free methane in matrix pores and adsorbed methane, in which free methane ① in the matrix can be calculated based on ideal gas state equation ③ and adsorbed methane ② can be calculated based on Langmuir adsorption equation. Since the volume is constant, the law of mass conservation can be written in the form of density conservation.

The flow of methane from the matrix to fracture follows Fick's law (Ren et al., 2017), and the gas flow diffusion rate Q is:

$$Q = -\frac{1}{\tau} \frac{M}{RT} \left(p_{mg} - p_{fg}\right) \tag{14}$$

where the desorption time τ is the time required when 63.2% of the total gas is desorbed, d; p_{mg} is methane pressure in matrix, MPa; p_{fg} is methane pressure in coal fracture, MPa. In Eq. (14), according to the law of mass conservation, the diffusion rate Q from coal matrix to fracture is equal to the change of methane in coal matrix in unit time. The Q depends on the concentration difference between matrix and fracture on the premise of constant desorption time. According to the ideal gas equation, the concentration difference is the internal and external pressure difference between the matrix and the fracture.

According to the mass conservation equation, the change rate of unit mass of methane in matrix is equal to the diffusion rate of methane, namely:

$$\frac{\partial}{\partial t}\left(\varphi_m \frac{M_g}{RT} p_{mg} + \frac{V_L b_L p_{mg}}{1 + b_L p_{mg}} \rho_c \rho_{gs}\right) = -\frac{1}{\tau} \frac{M_g}{RT} \left(p_{mg} - p_{fg}\right). \tag{15}$$

In Eq (15), the left side of the equal sign is the change of methane in the coal matrix in unit time, and the right side of the equal sign is the methane diffused from the matrix to the fracture in unit time. Thus, according to the conservation of mass, the mass change in unit space equals the mass difference between entering and leaving the space in unit time, and formula 15 can be obtained.

2) Methane and water flow in fracture

The fractures porosity is occupied by free methane and water. The change rate of free methane in the coal fractures in unit volume is equal to the difference of inflow from the matrix to fracture and outflow from fracture to wellbore (Fan et al., 2019a), defined as:

$$\overbrace{\frac{\partial}{\partial t}\left(s_g\varphi_f\frac{M}{RT}p_{mg}\right)}^{①}=\overbrace{\frac{1}{\tau}\frac{M}{RT}\left(p_{mg}-p_{fg}\right)}^{②}-\overbrace{\nabla\left(-\frac{\rho_f k k_{rg}}{\mu_g}\frac{M}{RT}\left(1+\frac{b_k}{p_{fg}}\right)\nabla p_{fg}\right)}^{③} \tag{16}$$

where s_g is gas saturation and s_w is water saturation, $s_g = 1\text{-}s_w$; ρ_f is free gas density in the fracture, kg/m^3; k is fracture permeability, mD; k_{rg} is gas relative permeability; μ_g is viscosity of methane, Pa·s, and; b_k is Klinkenberg coefficient, MPa. In Eq. (16), ① is the free gas content change in unit time in the fracture, which can be calculated by the ideal gas equation, ② is the diffusion in unit time from the matrix to the fracture, and ③ is the quality of the gas production in unit time from the fracture to the wellbore, which is derived quantitatively based on Darcy law.

The change rate of water in the fracture is equal to the outflow mass rate of water (Fan et al., 2019a):

$$\frac{\partial}{\partial t}\left(s_w\varphi_f\rho_w\right)=-\nabla\left(-\frac{\rho_w k k_{rw}}{\mu_w}\nabla p_{fw}\right) \tag{17}$$

where ρ_w is density of water in the fracture, kg/m^3; k_{rg} is water relative permeability; $\mu_w$is viscosity of water, Pa·s, and; p_{fw} is the fracture water pressure, p_{fw}=p_{fg}, MPa. In Eq. (17), the left side of the equal sign is the change of water in the fracture in unit time, and the right side of the equal sign is the water production from the fracture to the wellbore in unit time, which is also derived based on Darcy law.

The relative permeability of gas and water is based on the Corey equation (Fan et al., 2019a):

$$\begin{cases} k_{rg}=k_{rg0}\left(1-\dfrac{s_w-s_{wr}}{1-s_{wr}-s_{gr}}\right)^{\eta}\left(1-\left(\dfrac{s_w-s_{wr}}{1-s_{wr}-s_{gr}}\right)^{1+\frac{2}{\lambda}}\right) \\ k_{rw}=k_{rw0}\left(\dfrac{s_w-s_{wr}}{1-s_{wr}-s_{gr}}\right)^{\eta+1+\frac{2}{\lambda}} \end{cases} \tag{18}$$

where k_{rg0} is the endpoint relative permeability to gas; k_{rw0} is the endpoint relative permeability to water; s_{wr} is the irreducible water saturation; s_{gr} is the residual gas saturation; λ is the cleat size distribution index; η is the tortuosity coefficient for the relative permeability.

Table 6
Related parameters for the simulation (Fan et al., 2019a).

Parameter	Value	Parameter	Value
Initial pressure in fracture (pfg_o, MPa)	5.24	Adsorption time (τ,d)	4.34
Initial pressure in matrix (pmg_o, MPa)	5.24	Initial water saturation (S_w)	0.82
Langmuir volume of CH_4 (V_L, m^3/kg)	0.0196	Irreducible water saturation (S_{wr})	0.32
Langmuir strain constant (ε_L)	0.005	Residual gas saturation (S_{gr})	0.15
Langmuir strain constant (b_ε, MPa^{-1})	0.5	Klinkenberg factor (b_k, MPa)	0.36
Dynamic viscosity of CH_4 (μ_g, Pa·s)	1.03*10^{-5}	Entry capillary pressure (p_c, MPa)	0.1
Dynamic viscosity of water (μ_w, Pa·s)	1.01*10^{-3}	Cleat size distribution index (λ)	1.2
Initial permeability of fracture (k_o, mD)	1.0	Tortuosity coefficient (η)	1
Porosity of matrix (φ_m)	0.001	Fracture stiffness (K_n, MPa)	2800
Porosity of fracture (φ_f)	0.0423	Coal density (ρ_c, kg/m^3)	1350
Langmuir pressure of CH_4 (P_L, MPa)	1.32		

3) Governing equations for coal deformation

In CBM production the change in effective stress and the matrix shrinkage stress in methane desorption will cause the reservoir occurred deformation (Corey, 1954):

$$Gu_{k,ll}+\frac{G}{1-2v}u_{l,lk}-K\left(\frac{\varepsilon_L b_\varepsilon p_{mg}}{1+b_\varepsilon p_{mg}}\right)+f_k=0 \tag{19}$$

where G is the shear modulus, Pa; v is the v; K is the bulk modulus, Pa; f_k is the body force.

The purpose of the simulation is to explore the influence of changes in E and v caused by water production on permeability. Simulation parameters are referenced from Fan et al. (2019a) (Table 6), except for E and v. The evolution of E and v with water saturation follow Figs. 3 and 4. The evolution equation for permeability is Eq. (2). A geometric model 400 × 400 × 1m was established (Fig. 13), with the simulation parameters given in Table 6. The PDE and solid mechanics module in Comsol multiphysics were used in the simulation.

One point, 50 m away from the well, was used as fiducial points where permeability is monitored (Fig. 13). Since water production predominates in the early stages, the permeability change we follow is that caused exclusively by the change in effective stress - we ignore the effect of methane desorption on permeability evolution, and only simulate the first 600 days (water saturation is ~50% in 600th day) of CBM production as the water production stage (Kang et al., 2019; Fan et al., 2019a). The permeability increase caused by gas production is still considered in the simulation, not only the permeability decrease caused by water production.

The simulation result showed that As with the qualitative analysis (Fig. 14), considering the change of E and v with water production, the decrease in permeability with time is different from the permeability change under constant E and v under dry sample condition ($E0$ and $v0$) (Fig. 14). The reservoirs permeability with varying E and v decreases more rapidly than that with constant E and v (Fig. 14b–f), because the

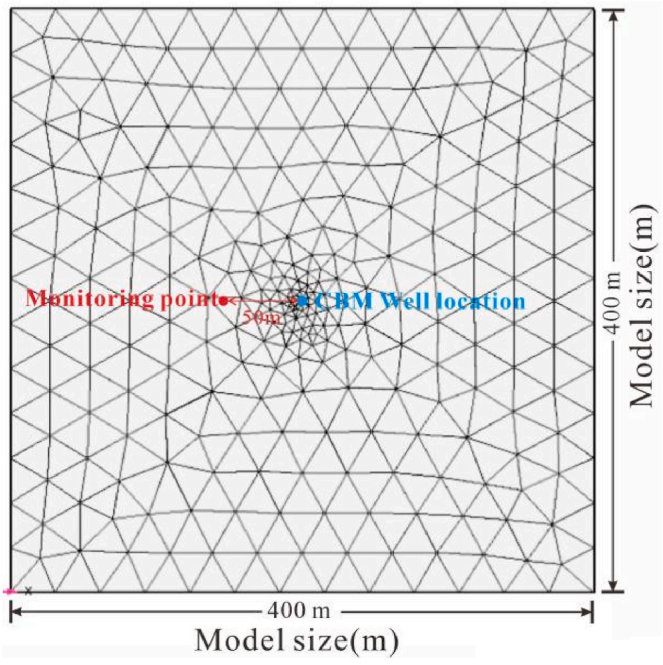

Fig. 13. Geometry and boundary conditions for model validation. The simulated boundary conditions are $\partial p_g/\partial x = 0$, $\partial S_w/\partial x = 0$, $\partial p_g/\partial y = 0$, $\partial S_w/\partial y = 0$.

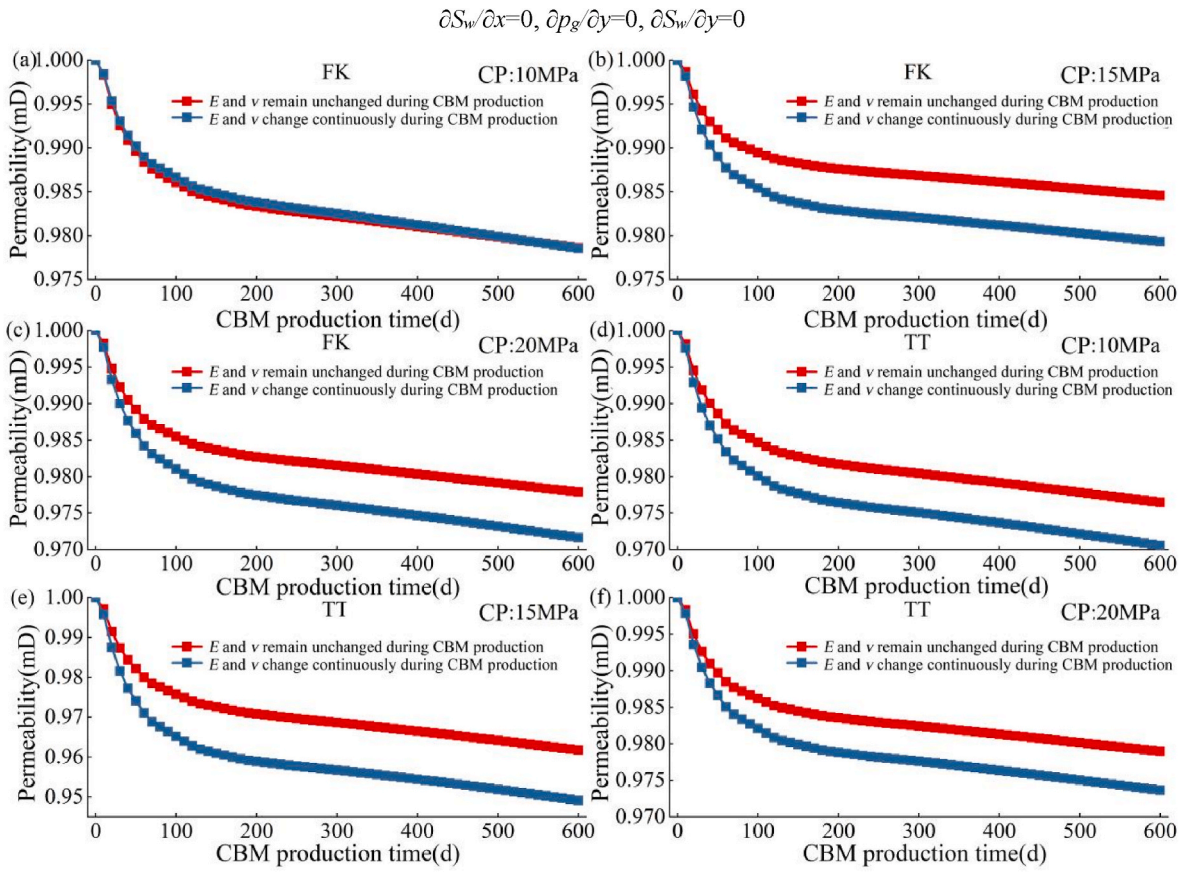

Fig. 14. Permeability comparison of E and ν change and unchange during CBM production.

change of E and ν leads to a greater decrease in permeability caused by water production (Fig. 6b–f). The FK-10MPa results showed that the permeability decreases more slowly with varying E and ν, although the difference was very small (Fig. 14a). This is because, for Fk-10MPa, the change of E and ν leads to less decrease of permeability caused by water production (Fig. 14a). The difference is very small because the E of FK-10MPa varies little with water saturation (Fig. 3a). This suggested that the change of E and ν caused by water production has a important influence on the change of permeability, and the influence trend depends on the size and change rate of E and ν.

Although the change of E and ν has an impact on the change of permeability, if the impact is small, it can be ignored without further analysis. Therefore, we need to quickly judge whether the change of E and ν on the change of permeability is worth further study. Triaxial compression tests on dry samples are the most common. We chose the variation data of E and ν of FK-15MPa as the data basis (the changes of E and ν of FK-15MPa are consistent with the overall change), and the changing trend of permeability under an $E0$ of 1000, 2000, 3000, 4000, 5000 MPa and the $\nu0$ of 0.15, 0.20, 0.25, 0.30, 0.35 were simulated. The influence of E and ν on permeability is determined by comparing the ratio of permeability difference and total permeability decline under dynamic and constant E and ν after 600 days. The difference of permeability is expressed as follows:

$$\Delta K = K_d - K_c \tag{20}$$

The influence degree is expressed as follows:

$$\eta = \frac{K_d - K_c}{K_0 - K_c} \times 100 \tag{21}$$

Where ΔK is permeability difference between dynamic and constant E and ν after 600 days, mD; K_d is the permeability under the dynamic

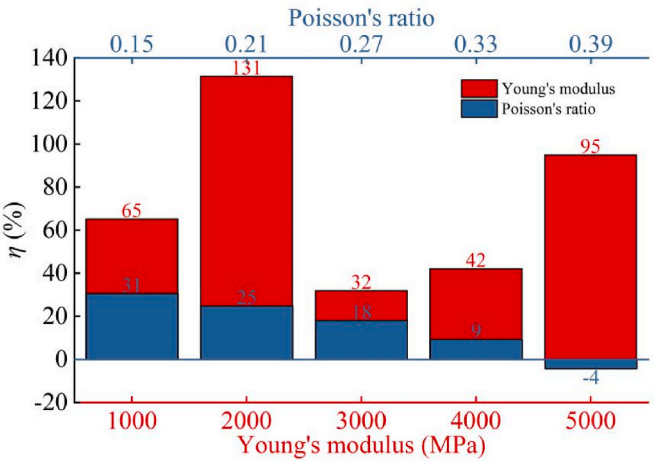

Fig. 15. Influence of different initial E and ν on permeability.

dynamic E and ν after 600 days, mD; K_c is the permeability under the constant E and ν after 600 days, mD; K_0 is the initial permeability, mD; η is the influence of dynamic E and ν on permeability change. If this value is small, it means that the change of E and ν has little influence on permeability.

The results showed that the variation of E can increase permeability change range by at least 32% and the maximum was more than 130% (Fig. 15), which indicates that if the change of E is taken into account, the permeability decrease will be 32% higher than the predicted permeability reduction, and the maximum will be more than 131%. This showed that the change of E in the process of water production has a

significant effect on permeability. It can also be seen that the influence degree of different initial E is different (Fig. 15). When the E is less than 3000 MPa and greater than 4000 MPa, the influence degree is greater, but when the E is 3000–4000 MPa, the influence of E change on permeability is small. The influence of ν change on permeability is smaller than that of E, which is no more than 31%, and gradually decreases with the increase of ν (Fig. 15). It can be concluded that the change of E change in CBM production significantly affects the change range of reservoir permeability, which needs to be considered. The change of ν also has an effect on the variation range of permeability, but the influence degree is lower than that E. The E of high volatility bituminous coal is generally less than 3 GPa (Perera et al., 2011; Masoudian et al., 2014; Ranathunga et al., 2016a, 2016b), thus the permeability changes caused by E in CBM production needs to be appropriately accommodated.

4. Conclusions

In view of the fact that the changes of Young's modulus (E) and Poisson's ratio (ν) and their influence on permeability in the CBM water production have been ignored by predecessors, we have carried out triaxial compression experiments and gas permeability experiments with different water saturation, combined with P&M permeability model and finite element method, analyzed the changes of E and ν and their influence on permeability. The main conclusions are as follows:

1) As water saturations decrease, E and ν of the coal reservoir increase linearly and decrease linearly, respectively, with variations of the order of ~25% and ~70%. This is because the water in the coal will dissolve the minerals in the coal and reduce the surface energy of the coal matrix, resulting in reservoir softening and deformation increase.
2) The effect of water on coal is affected by the in situ stress (confining pressure) and fractures. The effect of water on ν is reduced by the fractures in coal, but the effect of water on E is not significantly different from that of samples with fewer fractures. With the increase of confining pressure, the effect of moisture on E and ν increases gradually. This means that coal with fewer fractures and coal in high-stress areas are more sensitive to water.
3) The analysis based on the P&M permeability model and finite element method showed that there is no fixed trend in the change in permeability with decreasing water saturations, which depends on E and ν under initial water saturation and the rate of change with water saturation.
4) The variation of E can increase permeability change range by at least 32% and the maximum was more than 130%. When the E is less than 3000 MPa and greater than 4000 MPa, the influence degree is greater, more than 60%. The change of ν has less effect on the permeability change range, and the maximum value was 31%. This means that more attention should be focused on the influence of E and ν change with water production on permeability, especially the change of E.

Credit author statement

Junqiang Kang: Data curation, Writing- Original draft preparation, Methodology. **Xuehai Fu**: Conceptualization, Methodology, Software. **Derek Elsworth**: Writing- Reviewing and Editing. **Shun Liang**: Writing- Reviewing and Editing. **Hao Chen**: Writing- Reviewing and Editing.

Declaration of competing interest

The authors declare that they have no known competing financial interests or personal relationships that could have appeared to influence the work reported in this paper.

Acknowledgement

This work was supported by the National Natural Science Foundation of China (41772158, 42072190, 52174139, 41602174), the development of large oil and gas fields and CBM in major national scientific and technological projects (2016ZX05043-004-001), the Basic scientific research business fee of the China University of Mining and Technology (2020CXNL11).

References

Ali, M., Paul, S., Chatterjee, R., 2017. Cleat orientation from ground mapping and image log studies for in-situ stress analysis: coal bed methane exploration in south karanpura coalfield, India. Energy Fuel. 31 (7), 6812–6824. https://doi.org/10.1021/acs.energyfuels.7b00702.

Banerjee, A., Chatterjee, R., 2021. A methodology to estimate proximate and gas content saturation with lithological classification in coalbed methane reservoir, bokaro field, India. Nat. Resour. Res. 30, 2413–2429. https://doi.org/10.1007/s11053-021-09828-2.

Beaton, A., Langenberg, W., Pană, C., 2006. Coalbed methane resources and reservoir characteristics from the Alberta Plains, Canada. Int. J. Coal Geol. 65 (1–2), 93–113. https://doi.org/10.1016/j.coal.2005.04.013.

Chatterjee, R., Pal, P., 2010. Estimation of stress magnitude and physical properties for coal seam of rangamati area, raniganj coalfield, India. Int. J. Coal Geol. 81 (1), 25–36. https://doi.org/10.1016/j.coal.2009.10.006.

Chatterjee, R., Paul, S., 2013. Classification of coal seams for coal bed methane exploitation in central part of jharia coalfield, India - a statistical approach. Fuel 111, 20–29. https://doi.org/10.1016/j.fuel.2013.04.007.

Chatterjee, R., Paul, S., Pal, P., 2019. Relation between coalbed permeability and in-situ stress magnitude for coalbed methane exploration in Jharia and Raniganj coalfields, India. Lead. Edge 38 (10), 800–807. https://doi.org/10.1190/tle38100800.1.

Chen, L., Zhao, J., Zheng, Z., 2017. Acoustic emission characteristics of compressive deformation and failure of siltstone under different water contents. Ann. Mater. Sci. Eng. 4035487 https://doi.org/10.1155/2017/4035487.

Chen, S., Jiang, T., Wang, H., Feng, F., Yin, D., Li, X., 2019. Influence of cyclic wetting-drying on the mechanical strength characteristics of coal samples: a laboratory-scale study. Energy Sci Eng 7, 3020–3037. https://doi.org/10.1002/ese3.476.

Cheng, M., Fu, X., Kang, J., 2020. The compressibility of different pore and fracture structures and its relationship with heterogeneity and mineral in low rank coal reservoirs: an experimental study based on nuclear magnetic resonance and Micro-CT. Energy Fuels. https://doi.org/10.1021/acs.energyfuels.0c02119.

CMG, 2019. CMG Version 2019 User's Guide and Reference Guide.

Connell, L., Lu, M., Pan, J., 2010. An analytical coal permeability model for tri-axialstrain and stress conditions. Int. J. Coal Geol. 84, 103–114. https://doi.org/10.1016/j.coal.2010.08.011.

Corey, A., 1954. The interrelation between gas and oil relative permeability. Prod. Mon. 31, 38–41.

Cui, X., Bustin, R., 2005. Volumetric strain associated with methane desorption and its impact on coalbed gas production from deep coal seams. AAPG Bull. 89, 1181–1202. https://doi.org/10.1306/05110504114.

Dawson, G., Esterle, J., 2010. Controls on coal cleat spacing. Int. J. Coal Geol. 82, 213–218. https://doi.org/10.1016/j.coal.2009.10.004.

Eclipse, 2018. Eclipse Version 2018 User's Guide and Reference Guide.

Fan, C., Elsworth, D., Li, S., Chen, Z., Luo, M., Song, Y., Zhang, H., 2019a. Modelling and optimization of enhanced coalbed methane recovery using CO2/N2 mixtures. Fuel 253, 1114–1129. https://doi.org/10.1016/j.fuel.2019.04.158.

Fan, C., Elsworth, D., Li, S., Zhou, L., Yang, Z., Song, Y., 2019b. Thermo-hydro-mechanical -chemical couplings controlling CH4 production and CO2 sequestration in enhanced coalbed methane recovery. Energy 173, 1054–1077. https://doi.org/10.1016/j.energy.2019.02.126.

Freeman, D., Bush, D., 1983. Low permeability laboratory measurements by nonsteady state and conventional methods. Soc. Petrol. Eng. J. 23 (6), 928–936. https://doi.org/10.2118/10075-PA.

Fu, H., Tang, D., Xu, H., Xu, T., Chen, B., Hu, P., Yin, Z., Wu, P., He, G., 2016. Geological characteristics and CBM exploration potential evaluation: a case study in the middle of the southern Junggar Basin, NW China. J. Nat. Gas Sci. Eng. 30, 557–570. https://doi.org/10.1016/j.jngse.2016.02.024.

Gilman, A., Beckie, R., 2000. Flow of coal-bed methane to a gallery. Transport Porous Media 41, 1–16. https://doi.org/10.1023/A:1006754108197.

Gray, I., 1987. Reservoir engineering in coal seams, part 1-the physical process of gasstorage and movement in coal seams. SPE Reservoir Eng. 2, 28–34. https://doi.org/10.2118/12514-PA.

Green, M., Flanegan, K., Gilcrease, P., 2008. Characterization of a methanogenic consortium enriched from a coalbed methane well in the Powder River Basin, USA. Int. J. Coal Geol. 76 (1–2), 34–45. https://doi.org/10.1016/j.coal.2008.05.001.

Griffith, A., 1921. The phenomena of rupture and flow in solids. Philos. Trans. R. Soc. Lond. - Ser. A Contain. Pap. a Math. or Phys. Character 221, 163–198.

Gu, H., Tao, M., Cao, W., Zhou, J., Li, X., 2019. Dynamic fracture behaviour and evolution mechanism of soft coal with different porosities and water contents. Theor. Appl. Fract. Mech. 103, 102265. https://doi.org/10.1016/j.tafmec.2019.102265.

Gunter, W., Gentzis, T., Rottenfusser, B., Richardson, R., 1997. Deep coalbed methane in Alberta, Canada: a fuel resource with the potential of zero greenhouse gas emissions.

Energy Convers. Manag. 38, S217–S222. https://doi.org/10.1016/S0196-8904(96)00272-5.
Hamawand, I., Yusaf, T., Hamawand, S., 2013. Coal seam gas and associated water: a review paper. Renew. Sustain. Energy Rev. 22, 550–560. https://doi.org/10.1016/j.rser.2013.02.030.
Harpalani, S., Chen, G., 1995. Estimation of changes in fracture porosity of coal with gas emission. Fuel 74, 1491–1498. https://doi.org/10.1016/0016-2361(95)00106-F.
Jaeger, J., Cook, N., Zimmerman, R., 2009. Fundamentals of Rock Mechanics. John Wiley & Sons.
Jones, S., 1972. A rapid accurate unsteady-state klinkenberg permeameter. Soc. Petrol. Eng. J. 12 (5), 383–397. https://doi.org/10.2118/3535-PA.
Kang, J., Fu, X., Gao, L., Liang, S., 2018. Production profile characteristics of large dip angle coal reservoir and its impact on coalbed methane production: a case study on the Fukang west block, southern Junggar Basin, China. J. Petrol. Sci. Eng. 171, 99–114. https://doi.org/10.1016/j.petrol.2018.07.044.
Kang, J., Fu, X., Liang, S., Li, X., Chen, X., Wang, Z., 2019. A numerical simulation study on the characteristics of the gas production profile and its formation mechanisms for different dip angles in coal reservoirs. J. Petrol. Sci. Eng. 181, 106198. https://doi.org/10.1016/j.petrol.2019.106198.
Karthikeyan, G., Chand, J., Chatterjee, R., 2020. Impact of geomechanics in coal bed methane development and production, Barakar coals in central India. J. Petrol. Sci. Eng. 194, 107515. https://doi.org/10.1016/j.petrol.2020.107515.
Kędzior, S., 2009. Accumulation of coal-bed methane in the south-west part of the Upper Silesian Coal Basin (southern Poland). Int. J. Coal Geol. 80 (1), 20–34. https://doi.org/10.1016/j.coal.2009.08.003.
Lai, B., Li, H., Zhang, J., Jacobi, D., Georgi, D., 2016. Water-content effects on dynamic elastic properties of organic-rich shale. SPE J. 21, 635–647. https://doi.org/10.2118/175040-PA.
Laubach, S., Marrett, R., Olson, J., Scott, A., 1998. Characteristics and origins of coal cleat: a review. Int. J. Coal Geol. 35, 175–207. https://doi.org/10.1016/S0166-5162(97)00012-8.
Levine, J., 1996. Model study of the influence of matrix shrinkage on absolute permeability of coal bed reservoirs. Geological Society 109, 197–212. https://doi.org/10.1144/GSL.SP.1996.109.01.14.
Li, D., Hendry, P., Faiz, M., 2008. A survey of the microbial populations in some Australian coalbed methane reservoirs. Int. J. Coal Geol. 76 (1–2), 14–24. https://doi.org/10.1016/j.coal.2008.04.007.
Liu, H., Rutqvist, J., 2010. A new coal-permeability model, internal swelling stress and fracture–matrix interaction. Transport Porous Media 82, 157–171. https://doi.org/10.1007/s11242-009-9442-x.
Liu, J., Chen, Z., Elsworth, D., Qu, H., Chen, D., 2011. Interactions of multiple processes during CBM extraction: a critical review. Int. J. Coal Geol. 87, 175–189. https://doi.org/10.1016/j.coal.2011.06.004.
Liu, T., Lin, B., Fu, X., Gao, Y., Kong, J., Zhao, Y., Song, H., 2020. Experimental study on gas diffusion dynamics in fractured coal: a better understanding of gas migration in in-situ coal seam. Energy 195, 117005. https://doi.org/10.1016/j.energy.2020.117005.
Ma, T., Rutqvist, J., Oldenburg, C., Liu, W., Chen, J., 2017. Fully coupled two-phase flow and poromechanics modeling of coalbed methane recovery: impact of geomechanics on production rate. J. Nat. Gas Sci. Eng. 45, 474–486. https://doi.org/10.1016/j.jngse.2017.05.024.
Masoudian, M., Airey, D., El-Zein, A., 2014. Experimental investigations on the effect of CO2 on mechanics of coal. Int. J. Coal Geol. 128, 12–23. https://doi.org/10.1016/j.coal.2014.04.001.
Palmer, I., Mansoori, J., 1996. How permeability depends on stress and pore pressure in coalbeds: a new model. In: SPE Annual Technical Conference and Exhibition. https://doi.org/10.2118/36737-MS.
Pan, Z., Connell, L., 2012. Modelling permeability for coal reservoirs: a review of analytical models and testing data. Int. J. Coal Geol. 92, 1–44. https://doi.org/10.1016/j.coal.2011.12.009.
Pan, Z., Connell, L., Camilleri, M., 2010. Laboratory characterisation of coal reservoir permeability for primary and enhanced coalbed methane recovery. Int. J. Coal Geol. 82, 252–261. https://doi.org/10.1016/j.coal.2009.10.019.
Perera, M., Ranjith, P., Peter, M., 2011. Effects of saturation medium and pressure on strength parameters of Latrobe Valley brown coal: carbon dioxide, water and nitrogen saturations. Energy 36, 6941–6947. https://doi.org/10.1016/j.energy.2011.09.026.
Qin, Y., Moore, T., Shen, J., Yang, Z., Shen, Y., Wang, G., 2018. Resources and geology of coalbed methane in China: a review. Int. Geol. Rev. 60, 777–812. https://doi.org/10.1080/00206814.2017.1408034.
Ranathunga, A., Perera, M., Ranjith, G., 2016a. Influence of CO2 adsorption on the strength and elastic modulus of low rank Australian coal under confining pressure. Int. J. Coal Geol. 167, 148–156. https://doi.org/10.1016/j.coal.2016.08.027.
Ranathunga, A., Perera, M., Ranjith, P., Bui, H., 2016b. Super-critical CO2 saturation-induced mechanical property alterations in low rank coal: an experimental study. J. Supercrit. Fluids 109, 134–140. https://doi.org/10.1016/j.supflu.2015.11.010.
Ren, T., Wang, G., Cheng, Y., Qi, Q., 2017. Model development and simulation study of the feasibility of enhancing gas drainage efficiency through nitrogen injection. Fuel 194, 406–422. https://doi.org/10.1016/j.fuel.2017.01.029.
Robertson, E., Christiansen, R., 2006. A permeability model for coal and other fractured, sorptive-elastic media. In: SPE, Eastern Regional Meeting. https://doi.org/10.2118/104380-MS.
Roy, D., Singh, T., Kodikara, J., Das, R., 2017. Effect of water saturation on the fracture and mechanical properties of sedimentary rocks. Rock Mech. Rock Eng. 50, 2585–2600. https://doi.org/10.1007/s00603-017-1253-8.
Sampath, K., Perera, M., Elswort, D., Ranjith, P., Matthai, S., Rathnaweera, T., 2018. Experimental investigation on the mechanical behavior of victorian brown coal under brine saturation. Energy Fuels 32, 5799–5811. https://doi.org/10.1021/acs.energyfuels.8b00577.
Sawyer, W., Zuber, M., Kuuskraa, V., Horner, D., 1987. Using reservoir simulation and field data to define mechanisms controlling coalbed methane production. In: Proceedings of the 1987 Coalbed Methane Symposium, Alabama, pp. 295–307.
Seidle, J., 2011. Fundamentals of Coalbed Methane Reservoir Engineering. Penn Well Books.
Seidle, J., Jeansonne, M., Erickson, D., 1992. Application of matchstick geometry to stress dependent permeability in coals. In: SPE Rocky Mountain Regional Meeting. SPE Rocky Mountain Regional Meeting, pp. 18–21. https://doi.org/10.2118/24361-MS.
Shi, J., Durucan, S., 2004. Drawdown induced changes in permeability of coalbeds: a new interpretation of the reservoir response to primary recovery. Transport Porous Media 56, 1–16. https://doi.org/10.1023/B:TIPM.0000018398.19928.5a.
Shi, J., Durucan, S., 2005. A model for changes in coalbed permeability during primary and enhanced methane recovery. SPE Reservoir Eval. Eng. 8, 291–299. https://doi.org/10.2118/87230-PA.
Sinha, S., Gupta, S., 2021. A geological model for enhanced coal bed methane (ECBM) recovery process: a case study from the Jharia coalfield region, India. J. Petrol. Sci. Eng. 201, 108498. https://doi.org/10.1016/j.petrol.2021.108498.
Sun, Z., Li, X., Shi, J., Yu, P., Huang, L., Xia, J., Sun, F., Zhang, T., Feng, D., 2017. A semi-analytical model for drainage and desorption area expansion during coal-bed methane production. Fuel 204, 214–226. https://doi.org/10.1016/j.fuel.2017.05.047.
Ulusay, R., 2014. The ISRM Suggested Methods for Rock Characterization, Testing and Monitoring: 2007-2014. Springer.
Vasarhelyi, B., Van, P., 2006. Influence of water content on the strength of rock. Eng. Geol. 84, 70–74. https://doi.org/10.1016/j.enggeo.2005.11.011.
Vishal, V., Ranjith, P., Singh, T., 2015. An experimental investigation on behaviour of coal under fluid saturation, using acoustic emission. J. Nat. Gas Sci. Eng. 22, 428–436. https://doi.org/10.1016/j.jngse.2014.12.020.
Vutukuri, V., Lama, R., Saluja, S., 1974. Handbook on Mechanical Properties of Rocks. Trans. Tech. Publ, Clausthal, Germany.
Wang, S., Li, H., Wang, W., Li, D., 2018. Experimental study on mechanical behavior and energy dissipation of anthracite coal in natural and forced water-saturation states under triaxial loading. Arab J Geosci 11, 668. https://doi.org/10.1007/s12517-018-4014-4.
Yao, Q., Li, X., Zhou, J., Ju, M., Chong, Z., Zhao, B., 2015. Experimental study of strength characteristics of coal specimens after water intrusion. Arab J Geosci 8, 6779–6789. https://doi.org/10.1007/s12517-014-1764-5.
Wu, J., Feng, M., Han, G., Yao, B., Ni, X., 2018. Loading rate and confining pressure effect on dilatancy, acoustic emission, and failure characteristics of fissured rock with two pre-existing flaws. Comptes Rendus Mécanique 347 (1), 62–89. https://doi.org/10.1016/j.crme.2018.10.002.
Yao, Q., Chen, T., Ju, M., Liang, S., Liu, Y., Li, X., 2016. Effects of water intrusion on mechanical properties of and crack propagation in coal. Rock Mech. Rock Eng. 49, 1–11. https://doi.org/10.1007/s00603-016-1079-9.
Yu, G., Vozoff, K., Durney, D., 1993. The influence of confining pressure and water saturation on dynamic elastic properties of coals. Geophysics 58, 30–38. https://doi.org/10.1190/1.1443349.
Zhang, X., Wu, C., Wang, Z., 2019. Experimental study of the effective stress coefficient for coal permeability with different water saturations. J. Petrol. Sci. Eng. 182, 106282. https://doi.org/10.1016/j.petrol.2019.106282.
Zhou, B., Qin, Y., Yang, Z., 2020. Ion composition of produced water from coalbed methane wells in western Guizhou, China, and associated productivity response. Fuel 265, 116939. https://doi.org/10.1016/j.fuel.2019.116939.